The Origin of Reconnection-mediated Transient Brightenings in the Solar Transition Region

Shah Mohammad Bahauddin, Stephen J Bradshaw and Amy R Winebarger

The ultraviolet emission from the solar transition region is dominated by dynamic, low-lying magnetic loops. The enhanced spatial and temporal resolution of the Interface Region Imaging Spectrograph (IRIS) has made it possible to study these structures in fine detail. IRIS has observed "transient brightenings" in these loops, associated with strong excess line broadenings [1,2] providing important clues to the mechanisms which heat the solar atmosphere. However, the physical origin of the brightenings is debated. The line broadenings have been variously interpreted as signatures of nanoflares [3], magneto-hydrodynamic turbulence [4], plasmoid instabilities [5], and magneto-acoustic shocks [6]. In this Letter, we use IRIS slit-jaw images and spectral data, and the Atmospheric Imaging Assembly (AIA) of the Solar Dynamics Observatory (SDO), to show that the brightenings are consistent with magnetic reconnection mediated impulsive heating at field line braiding sites in multi-stranded transition region loops. The spectroscopic observations present evidence for preferential heating of heavy transition region ions and we show that this is consistent with ion cyclotron turbulence due to strong currents at the reconnection sites. Time-dependent differential emission measure (DEM) distributions are used to determine the heating frequency [7-9] and to identify pockets of faintly emitting "super-hot" plasma. The

observations we present and the techniques we demonstrate open a new avenue of diagnostics for reconnection mediated energy release in solar plasma.

IRIS has observed small scale (a few Mm) loop-like structures with intermittent brightenings in the Sun's active regions, which are associated with excess line broadenings [1,2]. These rapidly evolving brightenings are remarkably consistent with previous Hi-C observations of reconnection mediated heating in coronal loops [10]. Figure 1 (and Supplementary Figure 1) shows information revealed by IRIS regarding the geometries and the evolution of the brightened loops. Although SDO/AIA images and SDO/HMI magnetograms present these loops as singular, monolithic structures, having opposite polarity at their foot-points, unsharp masking applied to IRIS 1400 Å slit-jaw images demonstrates the existence of sub-structure within the brightening regions which we interpret as the loops being multi-stranded. The 131 Å and 94 Å SDO/AIA passbands detect a signature of the aftermath of heating at the braiding sites: "super-hot" plasma. The observations presented in Figure 2 and Figure 3 show a pixel-by-pixel analysis of the brightenings labeled 1 and 3 in Figure 1, and the evolution of their spectra. The IRIS 1400 Å channel is the primary mode for this analysis due to its fast cadence and high spatial resolution, and because it contains several lines readily available for plasma diagnostics. The intensity of Si IV 1403 Å emission varies strongly on the 50-100 second timescales over which the loops in Figure 2 and Figure 3 were rastered. This implies the presence of even faster variations below the timescale limit imposed by the rastering process. The density-sensitive O IV line ratio (1399.766 / 1401.157 Å, Supplementary Table 1) finds number densities of 10^{11} cm^{-3} in the brightenings and densities of 10^{13} cm^{-3} in the darker regions, which are more characteristic of the upper chromosphere (Extended Data Figure 1).

The Si IV 1403 Å line changes profoundly in the bright regions; it becomes multi-peaked (Figure 1, lower panel) and broadens substantially (FWHM $\Delta\lambda \approx 300$ km/s). We decomposed the Si IV 1403 Å profiles into two Gaussian components and found strong bi-directional flows with a maximum speed of 100 km/s toward and away from the observer. The two components of the bi-directional flows feature non-thermal components as large as 100 km/s (Figure 2 and Figure 3, panel Si IV(a) for the blue-shifted component and Si IV(b) for the red-shifted component). Strong Doppler shifts with broad non-thermal components are also observed in the S IV 1404 Å line profile. The down(surface)-ward flow observed in Si IV 1403 Å is somewhat slower than the up-ward flow to conserve momentum, since the atmosphere is gravitationally stratified. However, the O IV 1401 Å line profile is only ever weakly red-shifted (maximum 25 km/s) with a single component and no significant non-thermal broadening observed.

We conjecture the explanation for these different line profiles may lie in the formation temperatures of Si IV ($10^{4.8}$ K) and O IV (10^{5} K): Bi-directional jet material cools as it expands and so a stronger signature of the flow is observed in the lower temperature line; if the emission from O IV emanates from the slower, inner (and thus warmer) region of the reconnection jet, the Doppler-shifted components may not be sufficiently separable to resolve. Spectroscopic observations across a broader range of line formation temperatures than are currently available, and/or modeling and predictions of line profiles in non-equilibrium conditions for strong outflows, can address this matter in detail.

To further investigate the differences between the heavier (silicon and sulfur) ions, and lighter (oxygen) ion and their underlying cause, the ratio of the peak Si IV 1403 Å and O IV 1401 Å intensities is plotted for each pixel in Figure 2 and Figure 3 (top-right panel). This ratio is a strong diagnostic for non-equilibrium ionization and models show that enhanced values are induced by impulsive heating when density-dependent dielectronic recombination is included in the line formation process and ions with enhanced lifetimes are transported into denser layers of the atmosphere [11]. Large Si/O peak ratios are observed at the locations of the brightenings, indicating that non-equilibrium ionization physics driven by impulsive heating plays a key role in explaining the properties of the emission lines. To confirm this relationship, we extended our analysis to four more loops (Supplementary Figure 2 – 5) and present our results in a set of histograms (Supplementary Figure 6). Our findings are consistent with the analysis presented above for locations 1 and 3 of Figure 1.

We note here that non-equilibrium ionization alone cannot explain the Si IV line broadening relative to O IV. Bradshaw and Testa [11] showed that impulsive heating, coupled to non-equilibrium ionization and density-dependent dielectronic recombination, drives longer-lived ions formed at low temperatures into lower-lying, denser regions of the atmosphere, which causes them to emit more strongly (intensity scales as n^2) and has the net effect of increasing the Si IV/O IV intensity ratio. The emission is spread over a wider range of temperatures, but the range extends from the equilibrium formation temperature towards lower temperatures and favors narrower line widths. Thus, a mechanism which can substantially heat heavier ions preferentially to lighter ions, broadening the Si IV line profile relative to O IV, is required, which is also consistent with impulsive heating (e.g. by field-line braiding and reconnection) to explain the large Si IV/O IV intensity ratios.

The case for impulsive heating associated with the brightenings is strengthened by temporally correlating the IRIS emission with the hotter EUV emission [12] observed by AIA. Time-lags between the light curves of EUV channel pairs sensitive to different temperatures allow one to determine whether the plasma is heating or cooling [13-15]. Figure 4 (top) shows the light curves for loops at location 1 and 3 in the IRIS 1400 Å channel and six AIA EUV channels (131, 171, 193, 211, 335 and 94 Å). In both cases, the peak of the IRIS 1400 Å emission appears at least 20 seconds earlier than the AIA EUV emission peaks, providing further evidence that heating events are being observed. The light curves of the AIA EUV channels peak concurrently, indicating the short timescale of the events.

The properties of the emission measure (EM) distribution of the brightening loops yields information regarding timescales on which plasma is re-energized (heating frequency) [7-9,16] and on the presence of “super-hot” components to the emission [17-19] which are predicted, but hard-to-detect, signatures and evidence for impulsive heating [20,21]. Since the IRIS and AIA observations demonstrate the emitting volume along the line-of-sight is not isothermal then the differential emission measure (DEM) provides a more appropriate way to diagnose the heating properties. The two key properties of the DEM used to diagnose heating are its gradient cool-ward of the peak and an enhanced shoulder appearing above the temperature of the peak DEM. The heating frequency is related to the gradient of the DEM, where shallower (steeper) gradients suggest lower (higher) frequency events. An enhanced shoulder to the DEM indicates the presence of hot, but faint and hard-to-detect, emission associated with impulsive heating in loops prior to significant filling by ablation.

The evolving DEMs at locations 1 and 3 (Figure 1) are calculated using co-aligned data from the AIA EUV channels (see Methods) during the brightening events. The middle panel of Figure 4 shows that the DEMs broaden after the onset of each brightening in the IRIS 1400 Å channel (location 1: 600 s and location 3: 3000 s), and the gradient cool-ward of the peak steepens (gradients ≥ 3), indicating enhanced heating activity, and at the same time a hot ($T > 10$ MK) shoulder briefly appears, indicating strong impulsive heating. In the lower two panels of Figure 4 the gradient of the DEMs and the logarithms of the DEMs integrated above 14 MK are given with respect to time. A 2 – 3 orders of magnitude increase in the hot part of the emission measure is observed when IRIS sees the event and a sharp decrease in the DEM slope cool-ward of the peak is seen. We have computed the temporal evolution of the DEM-weighted temperature at the brightening/heating locations (Extended Data Figure 2) and found it transiently exceeds 10 MK at the onset of a brightening, which lends further support to the interpretation of impulsive heating creating hot plasma.

The 20 second time lag between the evolving AIA EUV light curves, and DEMs, and the IRIS 1400 A channel is consistent with timescales in numerical studies of simulated nanoflares where plasma is impulsively heated to multimillion degree temperatures [11]. To conclude our observational analysis, we propose the brief appearance of a hot shoulder to the DEMs is the first detected signature of high-temperature emission due to impulsive heating in non-flaring, low-lying, transition region loops.

The IRIS image intensity-gradient resolved data coupled with the AIA DEM analysis clearly show that the loop brightenings are associated with heating at the pixel locations where there is a strong concentration of sub-resolution strands. At the same pixels, the IRIS spectroscopic data show bi-directional flows, with strong non-thermal components, in the heavier ion lines (Si IV and S IV), while exhibiting no such features in the lighter ion line (O IV). Based on this observational evidence, we conjecture that plasma heating and the associated brightenings originate at braiding sites where strong currents exist and magnetic reconnection drives strong outflows, and where ion cyclotron waves leading to turbulence arise. Depending on the ratio of electron to ion temperature, and the ratio of number densities of the different species [22], each ion species in the multi-ion plasma must exceed a critical drift velocity to trigger the ion cyclotron instability and undergo heating by turbulence. We can show in the transition region that silicon and sulfur, in particular, have smaller drift velocities and thus shorter onset times for the instability. Consequently, they experience the strongest heating.

Our reasoning is based on the expectation that the magnetic field is close to force-free in the transition region, and strong currents and ion cyclotron waves arise at braiding sites, where the length of the current sheet is within the spatial scale of the observed structures (see Methods). Ion cyclotron waves are subject to instabilities which generate magnetic fluctuations that energize and scatter particles in random directions, resulting in electron and ion heating. In the case of ion cyclotron instabilities, the ion heating rate is weakly proportional to m_{ion} [22-24] and the critical drift velocity is smaller for the more abundant heavier ions. In Figure 5 we plot the ion heating rate for the most abundant heavy species (O, Si, S, Mg and Fe) in the transition region, for a temperature range between 0.01 to 0.05 MK, and show that the silicon and sulfur ions gain energy from the magnetic field at a significantly faster rate than the other species. This result demonstrates that heating by reconnection and ion cyclotron turbulence associated with the sites of magnetic braiding can provide a physical explanation for the observed high-intensity ratios of Si IV/O IV (heating) at the brightening sites associated with bi-directional flows (reconnection) and non-thermal broadening (turbulence).

We have also carefully ruled out several mechanisms that could explain some features of the observations including: thermal non-equilibrium (TNE) cycles under non-equilibrium ionization conditions (Supplementary Table 2 – 3), heating and line broadening by magneto-acoustic shocks (Extended Data Figure 3), and line broadening coupled with self-absorption in the Si IV line due to chromospheric reconnection (Extended Data Figure 4 – 5). The analysis is extended for the additional four loops as well (Supplementary Figure 7 – 10). In addition, the sound speed in the transition region (at $T \sim 10^5\ K$) is around $45\ km/s$ and so one may expect that shocks play a role in the heating process. However, the observed bidirectional flow speed peaks at 100 km/s. Under such conditions, even if all of the energy of the flow went into the ions then equating the thermal and kinetic energies yields a temperature increase of $\sim 10^5\ K\ (\ll 1\ MK)$, which is not sufficient to explain the observed line broadenings in Si IV and S IV, and cannot account for the lack of O IV line broadening.

References

1. De Pontieu, B. et al. The interface region imaging spectrograph (IRIS). *Sol. Phys.* **289**, 2733-2779 (2014).
2. Hansteen, V. et al. The unresolved fine structure resolved: IRIS observations of the solar transition region. *Science* **346**, 1255757 (2014).
3. Testa, P. et al. Evidence of nonthermal particles in coronal loops heated impulsively by nanoflares. *Science* **346**, 1255724 (2014).
4. De Pontieu, B. et al. On the prevalence of small-scale twist in the solar chromosphere and transition region. *Science* **346**, 1255732 (2014).

5. Innes, D. E., Guo, L. J., Huang, Y. M., & Bhattacharjee, A. IRIS Si IV line profiles: an indication for the plasmoid instability during small-scale magnetic reconnection on the Sun. *Astrophys. J.* **813**, 86 (2015).
6. De Pontieu, B., McIntosh, S., Martinez-Sykora, J., Peter, H., & Pereira, T. M. D. Why is non-thermal line broadening of spectral lines in the lower transition region of the sun independent of spatial resolution? *Astrophys. J. Lett.* **799**, L12 (2015).
7. Warren, H. P., Brooks, D. H., & Winebarger, A. R. Constraints on the heating of high-temperature active region loops: observations from Hinode and the Solar Dynamics Observatory. *Astrophys. J.* **734**, 90 (2011).
8. Winebarger, A. R. et al. Defining the “blind spot” of Hinode EIS and XRT temperature measurements. *Astrophys. J. Lett.* **746**, L17 (2012).
9. Warren, H. P., Winebarger, A. R., & Brooks, D. H. A systematic survey of high-temperature emission in solar active regions. *Astrophys. J.* **759**, 141 (2012).
10. Cirtain, J. W. et al. Energy release in the solar corona from spatially resolved magnetic braids. *Nature* **493**, 501-503 (2013).
11. Bradshaw, S. J., & Testa, P. Quantifying the Influence of Key Physical Processes on the Formation of Emission Lines Observed by IRIS. I. Non-equilibrium Ionization and Density-dependent Rates. *Astrophys. J.* **872**, 123 (2019).
12. Lemen, J. R. et al. The atmospheric imaging assembly (AIA) on the solar dynamics observatory (SDO). In *The solar dynamics observatory*, pp 17-40, (Springer, NY, 2011).
13. Viall, N. M., & Klimchuk, J. A. Evidence for widespread cooling in an active region observed with the SDO atmospheric imaging assembly. *Astrophys. J.* **753**, 35 (2012).

14. Lionello, R., Alexander, C. E., Winebarger, A. R., Linker, J. A., & Mikić, Z. Can large time delays observed in light curves of coronal loops be explained in impulsive heating?. *Astrophys. J.* **818**, 129 (2016).
15. Viall, N. M., & Klimchuk, J. A. The transition region response to a coronal nanoflare: forward modeling and observations in SDO/AIA. *Astrophys. J.* **799**, 58 (2015).
16. Bradshaw, S. J., Klimchuk, J. A., & Reep, J. W. Diagnosing the time-dependence of active region core heating from the emission measure. I. Low-frequency nanoflares. *Astrophys. J.* **758**, 53 (2012).
17. Barnes, W. T., Cargill, P. J., & Bradshaw, S. J. Inference of heating properties from “hot” non-flaring plasmas in active region cores. I. Single nanoflares. *Astrophys. J.* **829**, 31 (2016).
18. Cargill, P. J. Active region emission measure distributions and implications for nanoflare heating. *Astrophys. J.* **784**, 49 (2014).
19. Barnes, W. T., Cargill, P. J., & Bradshaw, S. J. Inference of heating properties from “hot” non-flaring plasmas in active region cores. II. Nanoflare trains. *Astrophys. J.* **833**, 217 (2016).
20. Cargill, P. J. Some implications of the nanoflare concept. *Astrophys. J.* **422**, 381-393 (1994).
21. Cargill, P. J., & Klimchuk, J. A. Nanoflare heating of the corona revisited. *Astrophys. J.* **605**, 911 (2004).
22. Forme, F. R. E., Wahlund, J. E., Opgenoorth, H. J., Persson, M. A. L., & Mishin, E. V. Effects of current driven instabilities on the ion and electron temperatures in the topside ionosphere. *J. Atmos. Terr. Phys.* **55**, 647-666 (1993).

23. Satyanarayana, P., Chaturvedi, P. K., Keskinen, M. J., Huba, J. D., & Ossakow, S. L. Theory of the current-driven ion cyclotron instability in the bottomside ionosphere. *J. Geophys. Res. Space Phys.* **90**, 12209-12218 (1985).

24. Marsch, E., Vocks, C., & Tu, C. Y. (2003). On ion-cyclotron-resonance heating of the corona and solar wind. *Nonlin. Processes Geophys.* **10**, 101-112 (2003).

Corresponding authors

Correspondence and requests for materials to S. M. Bahauddin.

Acknowledgements

This research was supported by the National Aeronautics and Space Administration (Grant: NNX15AF97A). The authors acknowledge the contributions of the LMSAL/IRIS science team and the NASA/SDO including the AIA, EVE, and HMI science teams for the observational data. IRIS is a NASA small explorer mission developed and operated by LMSAL with mission operations executed at NASA Ames Research Center and major contributions to downlink communications funded by ESA and the Norwegian Space Centre.

Author contributions

Shah Mohammad Bahauddin carried out the project as part of research towards the doctoral degree, including data analysis, interpretation and curation, formal analysis, and developing the necessary methodologies and validation schemes. Stephen J Bradshaw co-conceived the project and is a Co-I of the funding grant, undertook formal analysis, and supervised this work as part of SMB's doctoral thesis at Rice University. Amy R Winebarger co-conceived the project and is the PI of the funding grant. The original draft was written by Shah Mohammad Bahauddin, with revisions by Stephen J Bradshaw and Amy R Winebarger.

Author Information

Laboratory of Atmospheric and Space Physics, University of Colorado Boulder, Boulder, CO 80303, USA.

S M. Bahauddin

Department of Physics & Astronomy, Rice University, Houston, TX 77005, USA.

S. J. Bradshaw

Heliophysics and Planetary Science Office, NASA Marshall Space Flight Center, ZP 13, Huntsville, AL 35812, USA.

A. R. Winebarger

Main Figure Legends

Fig. 1: Co-aligned IRIS, SDO/AIA and SDO/HMI images of the observed loop brightenings and the associated spectra at the pixel locations of the brightenings. a, Candidate loop brightenings observed by SDO/AIA, SDO/HMI and IRIS: (from left to right columns) 131 Å SDO/AIA, 94 Å SDO/AIA, SDO/HMI magnetogram, 1600 Å SDO/AIA, IRIS 1400 Å and unsharp masked IRIS 1400 Å. The images in the top row were observed from 15:29:14 UTC to 15:32:53 UTC and the bottom row from 16:08:08 UTC to 16:14:49 UTC. **b**, Spectral information obtained from IRIS slit measurements for 3 locations: 1 and 3 where maximum brightening appears co-spatial with the loop; and 2 where there is no brightening. The O IV and S IV labels indicate the O IV 1404.157 Å and S IV 1404.808 Å emission lines respectively. **c,** Multi-peaked, broadened Si IV 1403 Å profile is fitted with a bi-component Gaussian (black, solid lines) for the brightening

regions at location 1 (top) and location 3 (bottom). The decomposed components are shown by black, dashed lines.

Fig. 2: Pixel-by-pixel analysis of the physical parameters along the magnetic loop structure observed at Location 1 in Figure 1. a, Temporal evolution (vertical axis) of Si IV intensity, Doppler components extracted from the fitted Si IV lines, Doppler shift from O IV lines, and the peak-to-peak intensity ratio of Si IV to O IV are shown for each pixel (horizontal axis). **b,** Temporal evolution (vertical axis) of intensity and the non-thermal components calculated from the widths of the Si IV, O IV and S IV lines are shown for each pixel.

Fig. 3: Pixel-by-pixel analysis of the physical parameters along the magnetic loop structure observed at Location 3 in Figure 1. a, Temporal evolution (vertical axis) of Si IV intensity, Doppler components extracted from the fitted Si IV lines, Doppler shift from O IV lines, and the peak-to-peak intensity ratio of Si IV to O IV are shown for each pixel (horizontal axis). **b,** Temporal evolution (vertical axis) of intensity and the non-thermal components calculated from the widths of the Si IV, O IV and S IV lines are shown for each pixel.

Fig. 4: Temporal evolution of the light curves and the differential emission measures (DEM) at the locations of loop brightenings. a, Light curves for the loops at location 1 **(left)** and location 3 **(right)** (Figure 1) are shown for the IRIS 1400 Å channel (black, solid lines) and six AIA EUV channels: 131 Å (blue), 171 Å (light-blue), 193 Å (green), 211 Å (yellow), 335 Å (red) and 94 Å (magenta). The vertical dashed lines indicate the times when the brightenings first appear in the IRIS 1400 Å channel and the vertical dotted lines indicate the times when the brightenings first appear in the SDO/AIA channels. **b,** Temporal evolution of the IRIS Si IV spectrum and the DEM distribution obtained from the AIA channels for loops at location 1 **(left)** and location 3

(right) are shown. **c,d,** Temporal evolution of the DEM slope cool-ward of the peak (black) and the integrated DEM (logarithmic) above 14 MK for loops (red) at (**c**) location 1 and (**d**) location 3 are presented. Solid lines indicate the lifetimes of the line broadenings at the brightening locations in the IRIS 1400 Å channel. The vertical dashed lines indicate the times when the brightenings first appear in the IRIS 1400 Å channel. Uncertainties associated with the measured quantities shown in **a,c,d** are in the range of 3% of the plotted values but not shown in the figure for the sake of readability.

Fig. 5: Heating rate due to the ion cyclotron instability for the most abundant heavy species (O, Si, S, Mg and Fe) in the transition region. Temperature change with respect to time due to the ion cyclotron instability is plotted for different initial temperatures (T_i). Black lines indicate cooler initial temperature ($T_i = 0.01\ MK$), while red lines indicate relatively higher temperatures ($T_i = 0.05\ MK$) from which the ions are heated. Solid, dashed, dot-dashed, dotted and dot-dot-dashed lines represent ions of Si IV, S IV, Mg IV, Fe IV, and O IV respectively.

Methods

The IRIS telescope feeds a far-UV (FUV: from 1332 Å to 1407 Å) and a near-UV (NUV: from 2783 to 2835 Å) band and the light passes through a spectrograph system to record spectral data [1]. The observation of interest is a large, coarse 8-step raster scan of active region AR12396. The scan was taken on 2015 August 06 from 15:19:21 to 16:41:59 UTC with an FOV of 14"x 119" at center location: x,y: -357",-369". The 0.33" x 119" slit was stepped 8 times with 2" steps and a step cadence of 9.1 seconds. However, this observation consists of the repetition of 68 such frames making the total raster cadence for each loop 73 seconds. Thus, the total number of raster scans is 544. The slit-jaw images (SJI) had an FOV of 120"x119" with a cadence of 36 seconds. Since the SJI cadence is four times longer than the raster cadence, there are 136 total slit-jaw images. All of the data are calibrated to level 2 by including dark current, flat-field, and geometric correction, and subsequently transformed to Level 3 data by building data cubes of spatially and temporally sequenced spectra.

The selection of suitable loops is based on two criteria: (1) the brightened arc is small enough to be considered a transition region loop (< 10 Mm) and (2) the intensity profile of the pixels is distinguishable above the noise threshold. However, since the raster scans through the entire image, it covers the loop only for a fraction of its evolution. Next, we extract the spectral data from the raster file. To determine line and continuum intensities, we fit each line profile by employing a double-peak Gaussian fitting algorithm with a background baseline. The baseline is first estimated within multiple shifted windows of width 200 separation units and by regressing the varying baseline to the window points, using a spline approximation, we adjust the baseline for the corresponding spectrum. Once the fitted spectrum was retrieved, we extracted the O IV 1399.766 Å, O IV 1401.157 Å, Si IV 1402.77 Å and S IV 1404.808 Å peaks. Here, the temporal lengths of the loops discussed in Figure 1 are 15:29:14 – 15:32:53 for Position 1 and 16:08:08 – 16:14:49 for Position 3 respectively.

For Figure 1, each frame of the IRIS SJI 1400 Å image is upsampled (bicubic interpolation) by a factor of 5 and sharpened by subtracting a blurred (unsharp) version of the image from itself (MATLAB built-in functions: imresize and imsharpen), similar to [10]. Since the new image is resized by a factor of 5, the standard deviation of the Gaussian low pass filter for unsharp masking is set to 5 (σ = 5 pixels). The strength of the sharpening effect for an edge pixel is set to

3. This value can be increased to introduce sharper contrast, however, an excessively large value for this parameter may create undesirable artifacts in the resulting image.

We extract observational parameters of physical significance, namely the peak ratio of the O IV 1401.157 Å and Si IV 1402.77 Å lines, and the Doppler shift and line width of O IV 1401.157 Å, Si IV 1402.77 Å, and S IV 1404.808 Å lines. The Si IV 1402.77 Å line did not exhibit single Gaussian or Lorentzian form, thus we adopted a bi-component Gaussian (since it fitted with minimum root mean squared error, which was always less than 3%) for this line and then measured the width and Doppler shift for each component. From the line width of the measured lines, we calculated the non-thermal broadening with the equation,

$$\Delta v_{NT} = \sqrt{\Delta v^2 - \Delta v_{Th}^2 - \Delta v_{inst}}$$

Where, Δv_{Th} is the maximum thermal line broadening at the peak formation temperature in the transition region. Note, a reliable component analysis could not be done for S IV bulk flow due to its weak signal strength and the presence of blending lines from O IV 1404.779 Å; thus, a single component analysis is performed and shown in Extended Data Figure 1.

We employ the atomic database Chianti [25] to calculate the theoretical intensity ratio of pairs of 1400 Å lines from the O IV ion as a function of density. We then interpolate our observation with this theoretical model and derive the density for each pixel, at each time step (Supplementary Information).

We have aligned the IRIS data to the AIA 1600 Å channel and the AIA 1600 Å channel to the other EUV channels using the solar limb (Extended Data Figure 6). Since our spatial scales are extremely small, we revise the co-alignments by trial and error and exclude any unrelated bright pixel in the region of interest. Finally, we isolated the pixel coordinates from the IRIS SJI image observed in the 1400 Å channel and the corresponding AIA EUV channels and integrated the pixel intensities to obtain the light curves.

We found that the peak of the IRIS 1400 Å emission appears at least 20 seconds earlier than the AIA EUV emission peaks. Although this timescale supports numerical studies from the literature [11], we present a back-of-the-envelope calculation to demonstrate its consistency: assuming a loop of $10\ Mm\ (10^{9}\ cm)$ in length and $10^{14}\ cm^{2}$ (width of strand below spatial resolution) in cross-section yields a volume of $V = 10^{23}\ cm^{3}$; if the density $n = 10^{11}\ cm^{-3}$ and the (initially low) plasma temperature increases by $dT = 5\ MK$ then the timescale (tau) is given, roughly, by $3\frac{k_B n dT}{\tau} = H$. Setting $H = 10\ erg\ cm^{-3}\ s^{-1}$ gives an energy input of $H \times V = 10^{24}\ erg\ s^{-1}$ and $\tau = 20\ seconds$. The total energy input is then $H \times V \times \tau = 2 \times 10^{25}\ erg$. Somewhat more powerful than the canonical nanoflare but still significantly weaker than a microflare, for example, for a set of very reasonable parameter values. Here, we've also assumed that energy redistribution by thermal conduction is, initially, relatively inefficient in the dense plasma, and radiative losses are small as the plasma reaches high temperatures quite quickly.

For the calculation of the DEM for each pixel, shown in Figure 4, we adopted the regularized inversion technique of Hannah & Kontar [26]. An IDL routine can be found in GitHub to efficiently implement this technique: https://github.com/ianan/demreg.

It is difficult to know for certain whether the magnetic field is force-free in the transition region observed by IRIS, or whether it is a better assumption in some parts of the Sun than in others (e.g. quiet Sun vs. active regions). While currents are needed to drive ion cyclotron waves, they need not be strictly field-aligned and so the field need not be exactly force-free. In addition, we point to the study conducted by Metcalf et al. [27] where the magnetic field in NOAA active region 7216 was measured and it was concluded that the field becomes force-free at a location in the chromosphere about 400 km above the photosphere, which is significantly below the heights we are considering.

Assuming a nearly force-free field, strong field-aligned currents at braiding sites in transition region loops could drive ion cyclotron waves at those locations. We can calculate the length of the current sheet for the structures of interest to us using the set of expressions for the Spitzer values [28],

$\eta = \frac{1}{3} L^2/\tau$ where L is the length of the current sheet and τ is the heating timescale

$\eta = 65.8\, T_e^{\frac{3}{2}} \ln \Lambda$ where T_e is the electron temperature and $\ln \Lambda$ is the slowly varying Coulomb logarithm.

In transition region, $T_e = 10^5\ K, \ln \Lambda = 15$ and observationally we found $\tau = 20\ s$ leading to $L = 1500\ km$, which is well within the spatial scale of the magnetic structures we are considering $\sim O(10\hat{}9)\ cm\ \cong 10{,}000\ km.$

As mentioned in the main text, ion cyclotron waves are subject to instabilities which generate magnetic fluctuations that energize and scatter particles in random directions, resulting in electron and ion heating [22]:

$$\left(\frac{\partial T_e}{\partial t}\right)^* = \frac{2}{3}\frac{m_e}{k_B} v_e^* V_{d,e}^2 \quad \text{for electrons;} \qquad (1)$$

$$\left(\frac{\partial T_i}{\partial t}\right)^* = \frac{2}{3}\frac{m_i}{k_B} v_i^* V_{d,e}^2 \quad \text{for ions.} \qquad (2)$$

Here v_e^*, v_i^* are the electron and ion collision frequency, respectively, and $V_{d,e}$ is the electron drift velocity. The heating can be initiated by the ion acoustic instability or the ion cyclotron instability. In the case of the ion acoustic instability:

$$\left(\frac{\partial T_i}{\partial t}\right)^* \propto \frac{1}{\sqrt{m_i}}$$

Lighter ions (e.g. O IV) are heated more rapidly than heavier ions (e.g. Si IV, S IV) resulting in greater excess line broadening in the lighter species, which we did not observe.

Since ion acoustic turbulence is not consistent with the observed O IV and Si IV line widths, we turn to a detailed examination of the ion cyclotron instability. The first step is to inspect the ratio of heating rates between O IV and Si IV ions initiated by ion cyclotron instability.

One can rewrite the rate of change of the ion temperature using the relationship $n_i m_i v_i^* = n_e m_e v_e^*$:

$$\left(\frac{\partial T_i}{\partial t}\right)^* = \frac{2}{3}\frac{m_e}{k_B}\frac{n_e}{n_i} v_e^* V_{d,e}^2 \qquad (3)$$

The threshold criterion for the instability is (according to [22]):

$$V_{d,e} > V_c = 15\frac{T_i}{T_e}V_{th,i} \tag{4}$$

At marginal stability:

$$V_{d,e} = V_c \tag{5}$$

The anomalous collision frequency is given by:

$$v_e^* = \alpha\, \Omega_i \left(\frac{V_{d,e}}{V_c} - 1\right)^2 \tag{6}$$

Where Ω_i is the cyclotron frequency:

$$\Omega_i = \frac{qB}{m_i c} \text{ rad/s [cgs]} \tag{7}$$

Clearly, we cannot evaluate (6) at marginal stability ($V_{d,e}$=V_c), since $v_e^* = 0$.

Therefore, express $V_{d,e}$ in multiples N of V_c, where N>1:

$$V_{d,e} = NV_c \tag{8}$$

Thus:

$$v_e^* = \alpha \frac{qB}{m_i c}(N-1)^2 \tag{9}$$

Substituting (8) and (9) into (3):

$$\left(\frac{\partial T_i}{\partial t}\right)^* = \frac{2}{3}\frac{m_e}{k_B}\frac{n_e}{n_i}\alpha\frac{qB}{m_i c}(N-1)^2 N^2 V_c^2$$

$$\left(\frac{\partial T_i}{\partial t}\right)^* = \frac{150 m_e}{k_B c}\frac{\alpha qB}{m_i}\frac{n_e}{n_i}\left(\frac{T_i}{T_e}\right)^2 (N-1)^2 N^2 V_{th,i}^2$$

$$\left(\frac{\partial T_i}{\partial t}\right)^* = \frac{150 m_e}{k_B c}\frac{\alpha qB}{m_i}\frac{n_e}{n_i}\left(\frac{T_i}{T_e}\right)^2 (N-1)^2 N^2 \frac{k_B T_i}{m_i}$$

$$\left(\frac{\partial T_i}{\partial t}\right)^* = \frac{150}{c}\alpha q B \frac{T_i^3}{T_e^2}\frac{m_e}{m_i^2}\frac{n_e}{n_i}\,(N-1)^2\,N^2 \qquad (10)$$

Taking the limit $N >> 1$:

$$\left(\frac{\partial T_i}{\partial t}\right)^* = \frac{150N^4\alpha q B}{c}\frac{T_i^3}{T_e^2}\frac{m_e}{m_i^2}\frac{n_e}{n_i} \qquad (11)$$

For a given pair of ions, the rate of (non-thermal) heating will depend on the relative magnitude for each ion of the quantity:

$$f_i = \frac{q_i T_i^3}{m_i^2 n_i} \text{ where } n_i = Y_i Ab n_H$$

Here, Y = ion population fraction, Ab = element abundance relative to hydrogen, and n_H = number density of hydrogen.

Since O IV and Si IV have the same charge then $q_{OIV} = q_{SiIV}$:

$$T_{OIV} \approx 1.58 \times 10^5 K \qquad T_{SiIV} \approx 8 \times 10^4 K$$

$$m_{OIV} = 2.66 \times 10^{-23} g \quad m_{SiIV} \approx 4.66 \times 10^{-23} g$$

Using the abundance set from Asplund [29] and Chianti ionization data [25]:

$$Ab(O) = \frac{10^{8.64}}{10^{12}} = 4.9 \times 10^{-4}\,,\; Ab(Si) = \frac{10^{7.51}}{10^{12}} = 3.24 \times 10^{-5}$$

$$Y_{OIV}(T_i) = 0.67\,, Y_{SiIV}(T_i) = 0.19$$

$$n_{OIV} = 0.67 \times 4.9 \times 10^{-4} n_H = 3.3 \times 10^{-4} n_H,$$

$$n_{SiIV} = 0.19 \times 3.24 \times 10^{-5} n_H = 6.2 \times 10^{-6} n_H$$

Now the ratio becomes:

$$\frac{f_{SiIV}}{f_{OIV}} = \frac{q_{SiIV}\, T_{SiIV}^3}{m_{SiIV}^2\, n_{SiIV}} \cdot \frac{m_{OIV}^2\, n_{OIV}}{q_{OIV}\, T_{OIV}^3}$$

$$= \frac{T_{SiIV}^3}{T_{OIV}^3} \frac{m_{OIV}^2}{m_{SiIV}^2} \frac{n_{OIV}}{n_{SiIV}}$$

$$= \frac{(8\times10^4)^3}{(1.56\times10^5)^3} \frac{(2.66\times10^{-23})^2}{(4.66\times10^{-23})^2} \frac{3.3\times10^{-4}}{6.2\times10^{-6}} = 2.25$$

This means quantitatively Si IV should be heated faster than O IV. Next, we calculate the magnitudes of the species heating rates due to ion cyclotron turbulence:

$$\left(\frac{\partial T_e}{\partial t}\right)^* = \frac{150 N^4 \alpha q B}{c} \frac{T_i^3}{T_e^2} \frac{m_e}{m_i^2}$$

Let the efficiency of the anomalous collision processes $\alpha = 10^{-3}$ [ref. 22] (since α is same for all interactions, the relative rates of temperature change between the ions remains the same. Consequently, the conclusion is independent of α) and $q = 1, B = 100G, \frac{T_i^3}{T_e^2} \sim 10^5\ K, \frac{m_e}{m_i^2} = \frac{9.11\times10^{-28}}{(1.67\times10^{-24})^2} = 3.27 \times 10^{20}$ with the assumption that the dominant electron-ion interaction is between e^- and H^+:

$$\left(\frac{\partial T_e}{\partial t}\right)^* = (7.85 \times 10^6) N^4$$

$$\left(\frac{\partial T_i}{\partial t}\right)^* = \left(\frac{T_i}{T_H}\right)^3 \left(\frac{m_H}{m_i}\right)^2 \frac{n_e}{n_i} \left(\frac{\partial T_e}{\partial t}\right)^*$$

Let the ion and hydrogen temperatures be the same initially. Let most of the electrons be due to hydrogen ionization. $T_i \sim T_H$, $n_e \sim n_H$:

$$\left(\frac{\partial T_i}{\partial t}\right)^* = \left(\frac{m_H}{m_i}\right)^2 \frac{n_H}{YAbn_H} \left(\frac{\partial T_e}{\partial t}\right)^*$$

$$\left(\frac{\partial T_i}{\partial t}\right)^* = \left(\frac{m_H}{m_i}\right)^2 \frac{q_f}{YAb} \left(\frac{\partial T_e}{\partial t}\right)^*$$

$m_{OIV} = 2.66 \times 10^{-22} g,\ q_f = 3$

$Y_{OIV} = 0.67\ \ Ab(O) = 4.9 \times 10^{-4}$

$$\left(\frac{\partial T_i}{\partial t}\right)^*_{OIV} = \left(\frac{1.67\times10^{-24}}{2.65\times10^{-23}}\right)^2 \frac{4}{0.67\times4.9\times10^{-4}} \left(\frac{\partial T_e}{\partial t}\right)^* = \mathbf{48}\left(\frac{\partial \boldsymbol{T_e}}{\partial \boldsymbol{t}}\right)^*$$

$m_{SiIV} = 4.66 \times 10^{-23} g,\ q_f = 3$

$Y_{SiIV} = 0.19\ Ab(Si) = 3.24 \times 10^{-5}$

$$\left(\frac{\partial T_i}{\partial t}\right)^*_{SiIV} = \left(\frac{1.67\times10^{-24}}{4.66\times10^{-23}}\right)^2 \frac{4}{0.19\times3.24\times10^{-5}} \left(\frac{\partial T_e}{\partial t}\right)^* = \mathbf{836}\left(\frac{\partial \boldsymbol{T_e}}{\partial \boldsymbol{t}}\right)^*$$

Dropping the previous assumption that T_i is at the equilibrium formation temperature of the line ($T_i = T_e$) and, instead, allowing the ion temperatures to be initially similar, we find that Si IV is heated at a rate greater than O IV by a factor $\frac{\mathbf{836}}{\mathbf{48}} \approx \mathbf{17}$. This can clearly account for the broader Si IV line widths.

The next step is to calculate the timescales of electron and ion heating by the ion cyclotron instability for different species. By integrating equation (1) and (2) and making substitutions from the expression of τ_{T_e}:

$$\tau_{T_e} \sim \frac{c}{150(N-1)^2 N^2 \alpha\beta q_e} \frac{T_e^3 m_i^2}{T_i^3 m_e}$$

$$\tau_{T_i} \sim \tau_{T_e} \frac{T_H^3}{T_e T_i^2} \frac{m_i^2}{m_H^2} \frac{n_i}{n_e} \frac{q_e}{q_i}$$

Let $B = 100G, T_e = 10^5\ K$ (close to the formation temperature of O IV and Si IV), and $T_{i=H} = 10^4\ K$. We list the heating timescales below:

$$\tau_{T_e}\ (N = 2, close\ to\ threshold) = 3\ seconds$$

$$\tau_{T_e}\ (N = 10, far\ from\ threshold) = 4.05 \times 10^{-6}\ seconds$$

And, for ions,

$$\tau_{T_{O\ IV}}\ (N = 2, close\ to\ threshold) = 6.1 \times 10^{-3}\ seconds$$

$$\tau_{T_{Si\ IV}}\ (N = 2, close\ to\ threshold) = 3.6 \times 10^{-4}\ seconds$$

Further away $(N = 10, far\ from\ threshold)$,

$$\tau_{T_{O\ IV}} = 9 \times 10^{-6}\ seconds$$

$$\tau_{T_{Si\ IV}} = 5.4 \times 10^{-7}\ seconds$$

Hence, even close to threshold, the timescale for the ion cyclotron instability for Si IV can be significantly less than 1 second and it is reasonable to suppose that the energy may be given to Si IV very rapidly before O IV (or the electrons) can be energized, leading to the line broadening of Si IV as observed.

Finally, the threshold condition for the ion cyclotron instability is:

$$V_{CC} = 15\ \frac{T_i}{T_e}\ V_{th,i}$$

And for the ion acoustic instability it is:

$$V_{CA} = \frac{T_i}{T_e}\ V_{th,e}$$

Therefore: $\frac{V_{cc}}{V_{ca}} = \frac{15V_{th,i}}{15V_{th,e}} = \frac{15\sqrt{\frac{k_B T_i}{m_i}}}{\sqrt{\frac{k_B T_e}{m_e}}} = 15\sqrt{\frac{T_i m_e}{T_e\, m_i}}$

Consequently, $\frac{V_{cc}}{V_{ca}} < 1$ and the threshold condition for the ion cyclotron instability would be met first. So, a plausible scenario is: At braiding sites, the favored ions (in this case Si and S) are heated strongly first (and the other ions and electrons weakly heated) by ion cyclotron turbulence and then the ion acoustic threshold is reached, which triggers further heating of lighter species if possible. We also expect thermalization and inter-species equilibration via collisions.

Methods Reference:

25. Del Zanna, G., Dere, K. P., Young, P. R., Landi, E., & Mason, H. E. CHIANTI–An atomic database for emission lines. Version 8. *Astron. Astrophys.* **582**, A56 (2015).

26. Hannah, I. G., & Kontar, E. P. Differential emission measures from the regularized inversion of Hinode and SDO data. *Astron. Astrophys.* **539**, A146 (2012).

27. Metcalf, T. R., Jiao, L., McClymont, A. N., Canfield, R. C., & Uitenbroek, H. Is the solar chromospheric magnetic field force-free? *Astrophys. J.* **439**, 474-481 (1995).

28. Ashbourn, J. M. A., & Woods, L. C. Energy transport in the solar transition layer. *Proc. Math. Phys. Eng. Sci.* **457**, 1873-1888 (2001).

29. Asplund, M., Grevesse, N., Sauval, A. J., & Scott, P. The chemical composition of the Sun. *Annu. Rev. Astron. Astrophys.* **47** (2009).

Data Availability

The observational data used for this study is designated as AR12396 tracking OBS 3860109180 (2015-08-06 15:19:21-16:41:59) and is publicly available for download from Lockheed Martin

Solar and Astrophysics Laboratory: https://iris.lmsal.com/search/. The co-aligned SDO data is also available at the above-mentioned web source. All data that support the findings of this study are available on reasonable request from the corresponding author.

Code availability

Details of the algorithms used to create the main figures, especially the unsharp masking and the calculation of ion cyclotron instability, is available in the methods section. The codes required to reproduce the results of these algorithms are available on reasonable request from the corresponding author. For the calculation of the DEM, an IDL routine written by Hannah & Kontar [26] is implemented and can be found in Git repository: github.com/ianan/demreg.

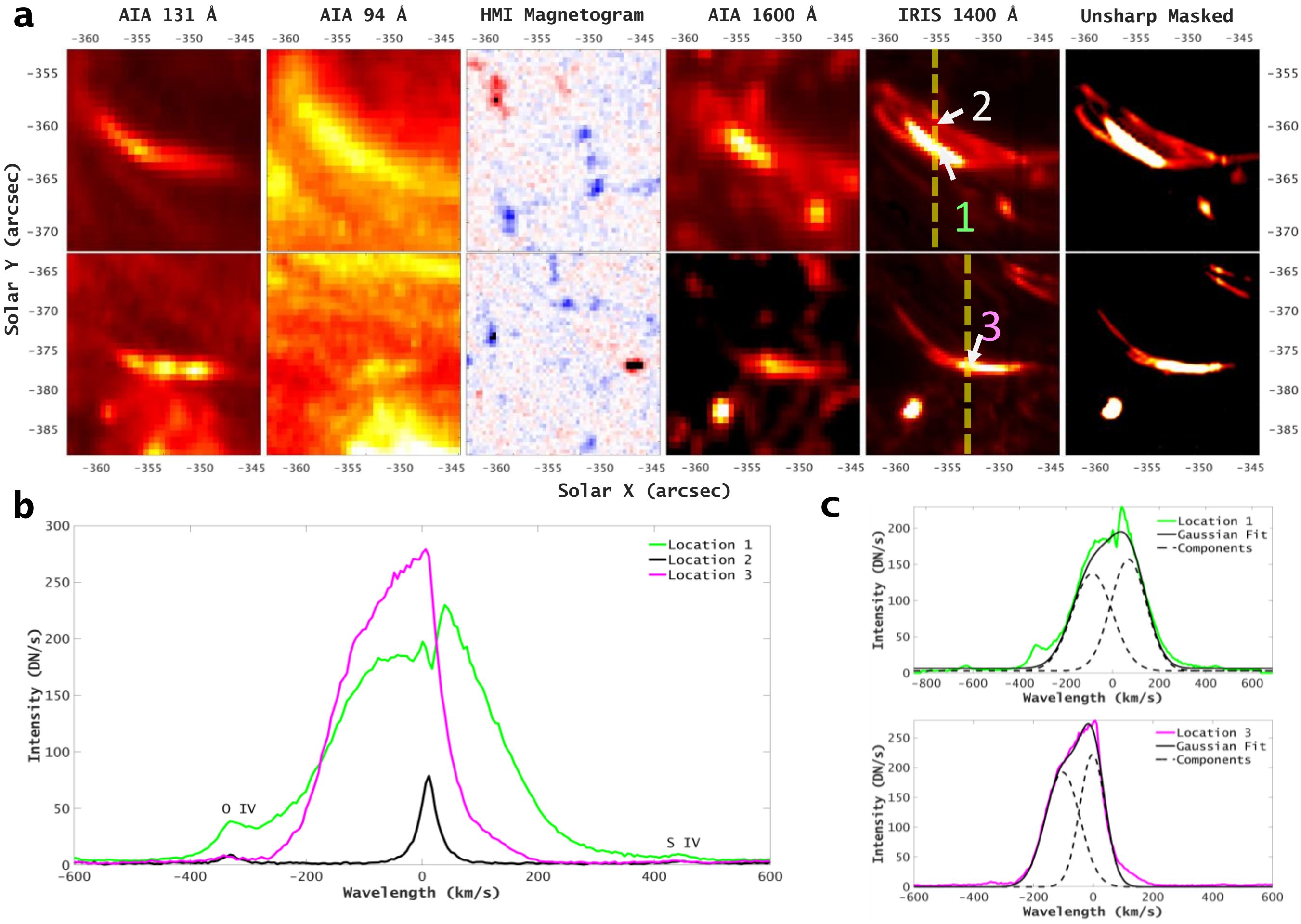
a
AIA 131 Å
AIA 94 Å
HMI Magnetogram
AIA 1600 Å
IRIS 1400 Å
Unsharp Masked
Solar Y (arcsec)
Solar X (arcsec)
1
2
3
b
O IV
S IV
Location 1
Location 2
Location 3
Intensity (DN/s)
Wavelength (km/s)
c
Location 1
Gaussian Fit
Components
Location 3
Gaussian Fit
Components
Intensity (DN/s)
Wavelength (km/s)

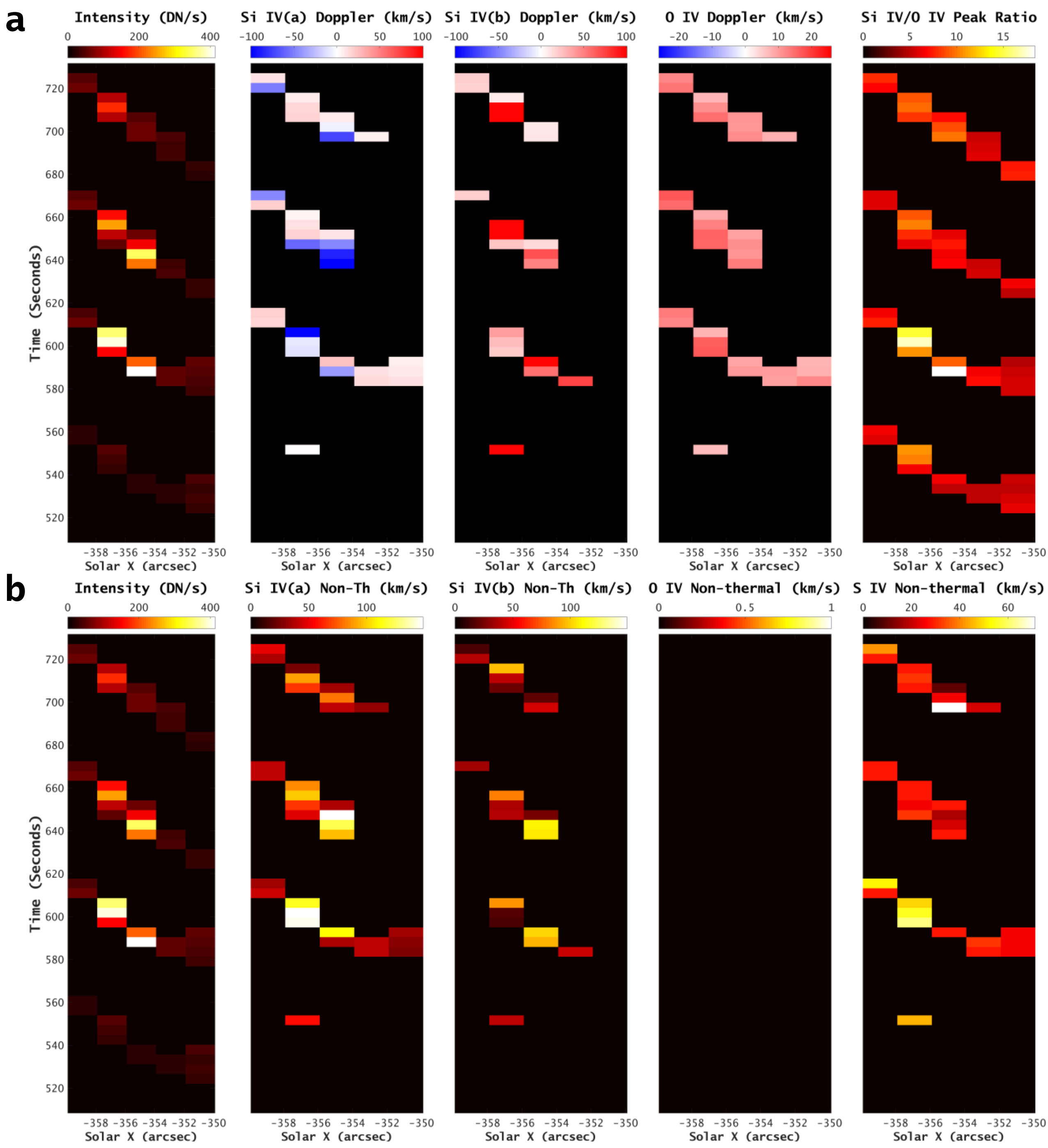

a
Intensity (DN/s)
Si IV(a) Doppler (km/s)
Si IV(b) Doppler (km/s)
O IV Doppler (km/s)
Si IV/O IV Peak Ratio
Time (Seconds)
Solar X (arcsec)
b
Intensity (DN/s)
Si IV(a) Non-Th (km/s)
Si IV(b) Non-Th (km/s)
O IV Non-thermal (km/s)
S IV Non-thermal (km/s)
Time (Seconds)
Solar X (arcsec)

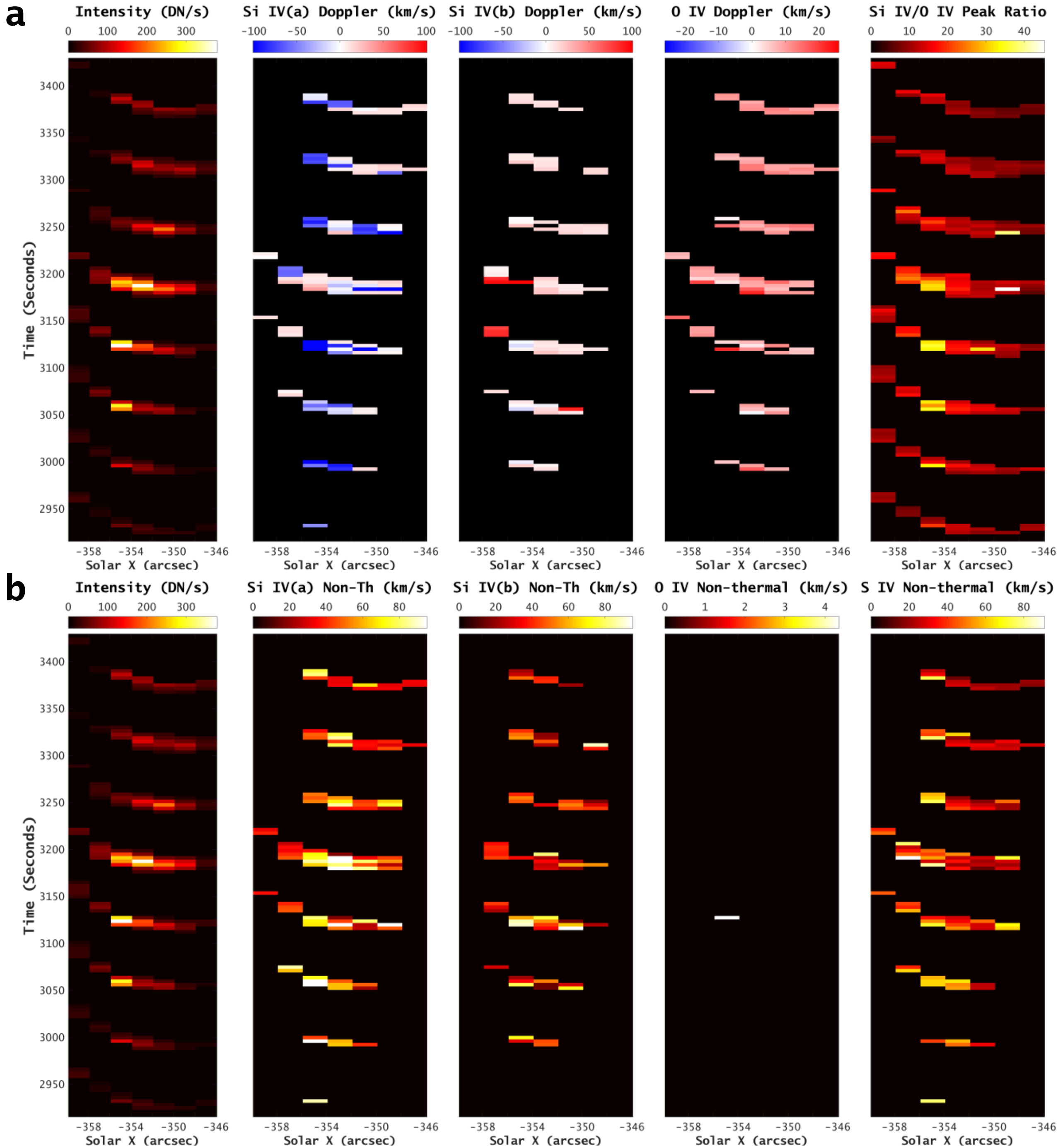
a
Intensity (DN/s)
Si IV(a) Doppler (km/s)
Si IV(b) Doppler (km/s)
O IV Doppler (km/s)
Si IV/O IV Peak Ratio
Time (Seconds)
Solar X (arcsec)
b
Intensity (DN/s)
Si IV(a) Non-Th (km/s)
Si IV(b) Non-Th (km/s)
O IV Non-thermal (km/s)
S IV Non-thermal (km/s)
Time (Seconds)
Solar X (arcsec)

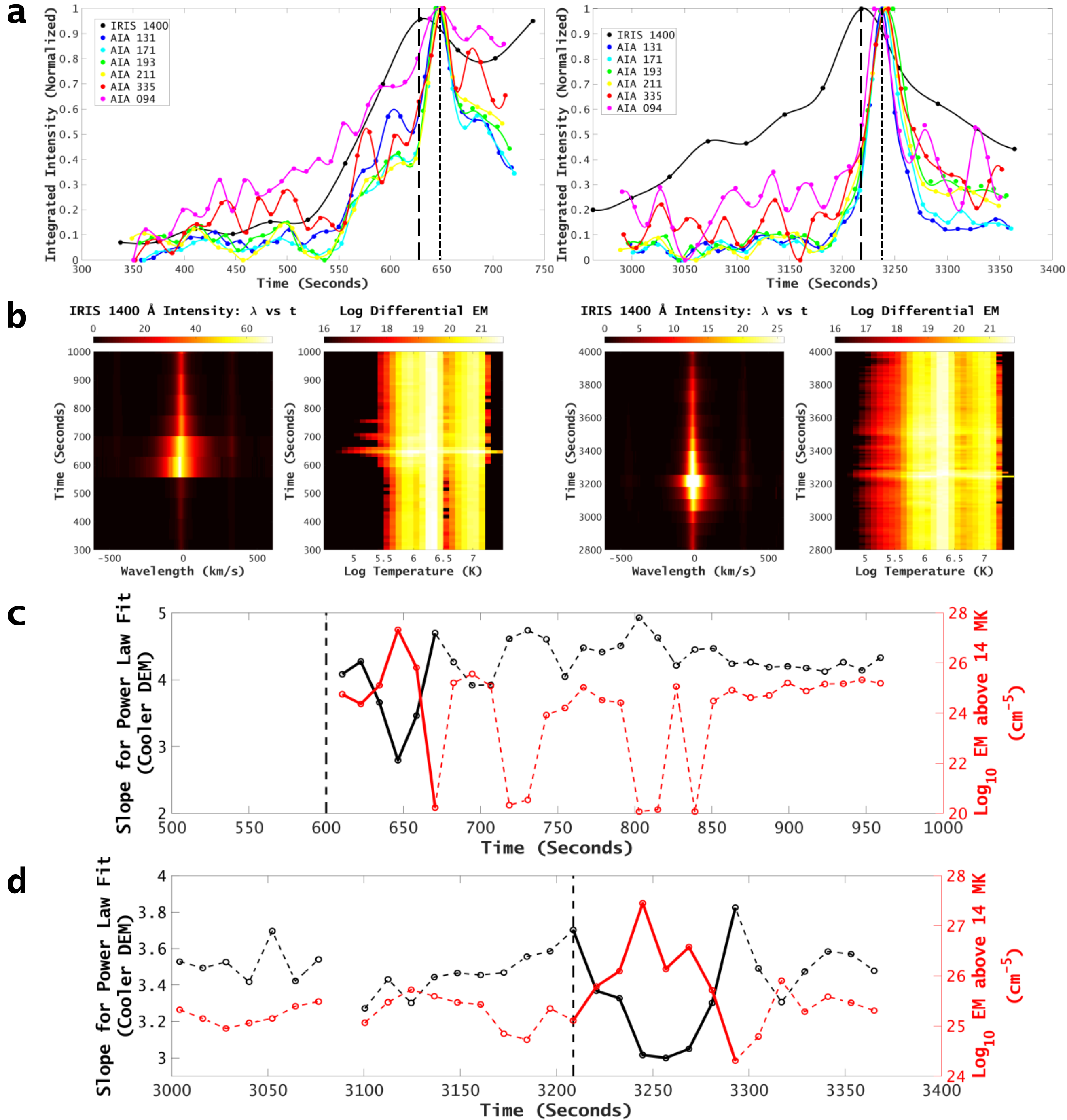
a
Integrated Intensity (Normalized)
Time (Seconds)
IRIS 1400
AIA 131
AIA 171
AIA 193
AIA 211
AIA 335
AIA 094
b
IRIS 1400 Å Intensity: λ vs t
Log Differential EM
Time (Seconds)
Wavelength (km/s)
Log Temperature (K)
c
Slope for Power Law Fit (Cooler DEM)
Log10 EM above 14 MK (cm^-5)
Time (Seconds)
d
Slope for Power Law Fit (Cooler DEM)
Log10 EM above 14 MK (cm^-5)
Time (Seconds)

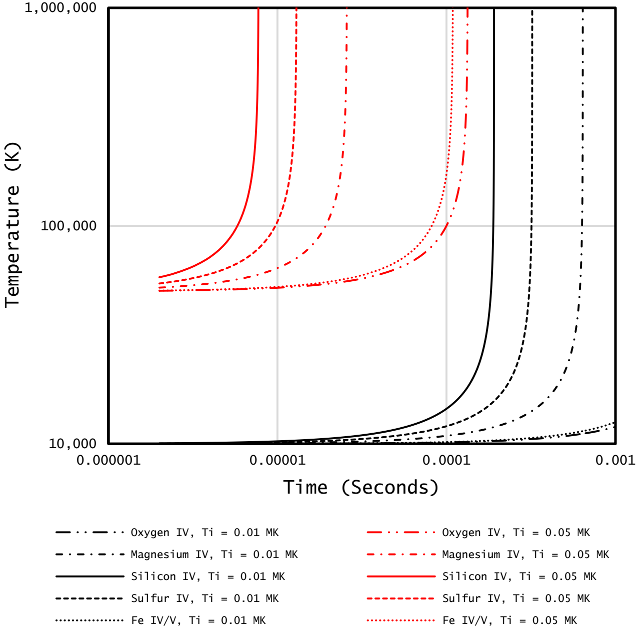

1,000,000
100,000
10,000
0.000001
0.00001
0.0001
0.001
Temperature (K)
Time (Seconds)
Oxygen IV, Ti = 0.01 MK
Magnesium IV, Ti = 0.01 MK
Silicon IV, Ti = 0.01 MK
Sulfur IV, Ti = 0.01 MK
Fe IV/V, Ti = 0.01 MK
Oxygen IV, Ti = 0.05 MK
Magnesium IV, Ti = 0.05 MK
Silicon IV, Ti = 0.05 MK
Sulfur IV, Ti = 0.05 MK
Fe IV/V, Ti = 0.05 MK